Article

A Numerical Procedure for Variable-Pitch Law Formulation of Vertical-Axis Wind Turbines

Cinzia Rainone, Danilo De Siero, Luigi Iuspa [ID], Antonio Viviani [ID] and Giuseppe Pezzella *[ID]

Engineering Department, Università della Campania "L.Vanvitelli", Via Roma 29, I-81031 Aversa, CE, Italy
* Correspondence: giuseppe.pezzella@unicampania.it

Abstract: A numerical procedure was developed to determine a variable-pitch law that maximized the performance of a vertical-axis wind turbine (VAWT). The methodology was based on the determination, for each blade, of the angle of attack maximizing the stationary aerodynamic efficiency at prescribed azimuthal positions. The angles of attack were determined by means of a panel method with a low computational effort, and the methodology was implemented in Matlab$^{®}$ software (version R2021a) allowing us to achieve in real time a variable-pitch law suitable for the turbine geometry. The variable pitch law was validated by considering its effect on the torque of a 2D model of an H-Darrieus turbine. U-RANS analyses were carried out with a $K - \omega \, SST$ model and a sliding-mesh technique was used to prescribe the blade motion around the shaft and pitch motion. Results showed how the variable-pitch law delayed the dynamic stall and improved the aerodynamic performance considerably.

Keywords: wind energy; vertical-axis wind turbine; variable-pitch law; computational fluid dynamics

1. Introduction

The reduction of pollutant emissions from fossil combustion and the need for a valid alternative to fossil fuels, due to an increasing demand of coal and natural gas resources, have motivated the European Union (EU) to invest into research on renewable energy. EU has established that renewable energy contribution will be 20% higher than the current amount and at least one-third of this production could be possibly derived from wind energy within the 2020s [1,2]. The technological progress achieved in the renewable energies field has been relevant and, in particular, wind power has become the main renewable energy source in many countries.

Wind turbines represent the main technology able to convert kinetic energy extracted from the wind into electric energy [3,4]. Wind turbines are exposed to various environmental conditions during their operating life (i.e., wind/dust, rain, hail, snow, ice formation, ultraviolet exposure). These operating conditions combined with blade tip speeds result in damage to the leading edge due to leading edge erosion (LEE) effect [5]. There are several studies in the literature about the mechanisms, modelling, and possibilities of preventing the surface erosion of wind turbine blades [6,7].

Wind turbines are classified as horizontal-axis wind turbine (HAWT) and vertical-axis wind turbine (VAWT), according to the spatial orientation of the rotating axis. In the last years, an increasing interest in vertical-axis wind turbine has been experienced because this configuration presents some relevant advantages compared to the horizontal-axis layout. Specifically, it is able to work with an omnidirectional asymptotic velocity without a yaw mechanism that generates power loss. This configuration is also more compact and less noisy [8]. Moreover, with the prospective of urban application, the micro-VAWT can represent a valid alternative to photovoltaic devices.

On the other hand, VAWT is less efficient compared to HAWT, due to the presence of unsteady aerodynamic phenomena, e.g., dynamic stall, deep stall, and blade–wake

interaction. The steep variation in time of the angle of attack is among the main causes of the dynamic stall phenomenon, which increases the noise and the fatigue life of the turbine components [9,10]. The delay of the dynamic stall phenomenon has been the subject of study in recent years, and different strategies have been considered in literature. Wang et al. [11] proposed a new technology based on flexible blades. According to Huang's research [12], blade sections are able to change automatically their camber angle to prevent flow separation. These effects were noticed by Bishop [13] and by Swartz et al. [14] when studying flying squirrels and bats, which are able to fly at high angles of attack by changing the shape of their wings during the flapping flight. Furthermore, Ismail and Vijayaraghavan [15] proposed a combination of semicircular inward dimple and a Gurney flap at the surface of a Darrieus turbine. They observed that the adoption of an optimized combination of a Gurney flap and a dimple produced an increase of the tangential component of the aerodynamic force. Another strategy, adopted to delay the dynamic stall, is an application of turbulators [16] or vortex generators [17,18] on the surface of the blades. These technologies energize the boundary layer making the flow turbulent and reducing the size of the laminar bubble with a consequent rapid reattachment of the flow. Even though turbulators and vortex generators are cheap technologies, they present main cons: (i) the right position on the surface of the blades is difficult to find because it is influenced by the variation of the angle of attack; (ii) the turbulent boundary layer creates extra friction drag [19,20].

Another technology often used to reduce the variation in time of the angle of attack is an active pitch system. Paraschivoiu et al. [21] and Rezaeiha et al. [22] studied the effect of a fixed-pitch angle on the aerodynamic performance of a turbine. However, according to that approach, blade sections do not operate at an optimum angle of attack at each azimuthal position. Indeed, turbine performance can be improved further by utilizing a variable-pitch mechanism. Generally, a linkage mechanism is the most used for this purpose. It is characterized by main links that rotate around the main rotational point, and secondary links that rotate around an eccentric rotational point. This way, the blades are controlled in order to avoid the stall and also maintain a favourable angle of attack. Even if a linkage mechanism is able to improve power generation with respect to a fixed-pitch configuration, the blade sections operate at angles of attack which are not optimum in most azimuthal positions [23,24]. Moreover, the determination of link lengths and eccentric rotational point position requires an optimization process, namely, the best combination of variables whose performance improvement is not known a priori. Therefore, this system is not versatile because it is necessary to execute an optimization at any variation of the operating conditions.

Different methodologies to define a variable-pitch law are presented in literature. Hwang et al. [25] proposed an optimization procedure to determine the optimal pitch angle at specific azimuthal positions. Computational fluid dynamics (CFD) was adopted to estimate the aerodynamic performance coupled with a genetic algorithm optimizer. The optimal variable-pitch law improved the power generation by 25% with respect to the one obtained with the cycloidal motion. Paraschivoiu et al. [21] analysed a two-blade H-Darrieus turbine modelling a variable-pitch law with an analytical function whose coefficients were used as optimization process variables. The aerodynamic model used to determine the performance was a double-multiple streamtube (DMS), while the optimization was carried out by using a genetic algorithm. The results showed an increase in the power generation at different tip-speed ratio (TSR). Both methodologies reported above required a high computational effort and should execute at the variation of the operating conditions. Conversely, Staelens et al. [26] proposed three different methodologies, computationally more efficient, to define a variable-pitch law. The first imposed the local angle of attack of airfoils equal to the stall angle value throughout the rotation of the turbine. Although they obtained an increase of efficiency for a higher wind speed, the variation in time of the angle of attack was physically impossible because it presented discontinuity at azimuthal positions $0°$ and $180°$. The second methodology proposed to replace the value of

the angle of attack with the value of the angle of stall when the former exceeded the latter. Although the aerodynamic performance decreased, the variation of the attack angle was smoother than the previous one but it still presented discontinuities. The last methodology proposed a sinusoidal correction function whose amplitude was equal to the maximum difference between the local angle and the static stall angle. This way, the local angle of attack had a continuous variation in time with respect to the cyclical condition. Although these methodologies allowed an improvement of the aerodynamic performance, the blade worked in an unstable condition because the angles of attack were close to the angle of stall, and aerodynamic performance could drop dramatically due to flow separation.

In the present work, a variable-pitch law that makes each blade section, namely, airfoil, able to operate at the conditions of the maximum steady aerodynamic efficiency, is presented. The proposed methodology is computationally efficient compared to equivalent approaches found in the literature. In fact, for eight azimuthal positions, the static polars of the airfoil are calculated using a potential solver, and the effective angles of attack that maximize steady efficiency are determined. The angle by which each blade section must rotate to operate at an effective angle of attack is the pitch angle. A cubic interpolation of pitch angles produces a variable-pitch law. The automatic procedure was implemented in Matlab software.

2. Aerodynamics of VAWT

A schematic representation of a VAWT is reported in Figure 1. A polar reference system (R, θ) having its origin in the centre of the shaft is used to represent the current blade position.
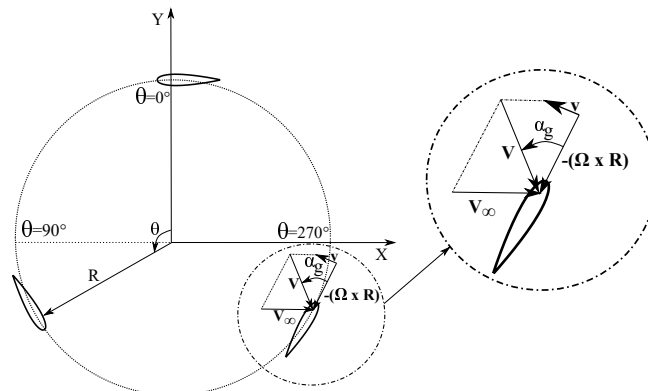
Figure 1. Two-dimensional view of a three-bladed rotor, showing the velocity triangles.

The flow field on a blade is characterized by different velocity types: (i) a tangential velocity component due to rotation $(-\mathbf{\Omega} \times \mathbf{R})$ where $\mathbf{\Omega}$ is the rotational velocity and $\mathbf{R}$ is the radius vector; (ii) an asymptotic wind velocity $\mathbf{V}_\infty$; (iii) an induced velocity $\mathbf{v}$. According to Figure 1, the sum of those velocities returns the relative velocity of a single blade:

$$\mathbf{V} = \mathbf{V}_\infty - (\mathbf{\Omega} \times \mathbf{R}) + \mathbf{v} \tag{1}$$

As the turbine rotates, both magnitude and direction of the relative velocity change cyclically. Therefore, the angle between the airfoil chord and the relative velocity, namely, the geometric angle of attack (α_g), follows the same cyclical variation. The geometric angle of attack can be expressed, neglecting for simplicity the small induced velocity $\mathbf{v}$, as a function of azimuthal position (θ) as:

$$\alpha_g = \arctan\left(\frac{\sin \theta}{\lambda + \cos \theta}\right) \tag{2}$$

where λ is the tip-speed ratio (TSR) defined by:

$$\lambda = \frac{\Omega R}{V_\infty} \tag{3}$$

The parameter that gives knowledge about the three-dimensionality of the flow is the aspect ratio (AR), defined as:

$$AR = \frac{b}{c} \tag{4}$$

where b is the blade span while c is the chord of the airfoil. By assuming an AR greater than 7.5, three-dimensional effects can be neglecting [27,28]. The aeronautical convention is adopted for α_g, i.e., positive values of α_g are associated to anticlockwise rotations of the relative velocity with respect to the airfoil chord, as shown in Figure 2. To ensure an effective operating condition of the turbine, the suction side of the i-th airfoil is oriented toward the rotor centre, as shown in Figure 2.
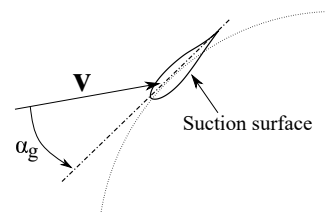
Figure 2. Positive angle of attack.

An inverse proportionality relation links the TSR values with the values of α_g [10]. Low values of the TSR relate to steep variations of the α_g and vice versa. Steep changes in time of α_g, and a high frequency oscillation of airfoils (pitching motion) create an unsteady flow field on turbine blades, known as the dynamic stall condition [29]. As reported in the literature [30], the dynamic stall is characterized by the development and interaction of vortical structures of different sizes generated on the airfoil's suction surface. Blades experience an increase of the lift force for values of the angle of attack far beyond the static stall angle. This phenomenon occurs when the leading edge vortex (LEV) spans over the whole suction surface side. Consequently, when the airfoil approaches its maximum angle of attack, the LEV detaches from the airfoil causing a sudden lift stall and a consequent rapid increase of drag [31,32].

In Figure 3, a schematization of the aerodynamic forces acting on an airfoil is reported. Tangential (**T**) and normal (**N**) forces are related to lift (**L**) and drag (**D**) forces, respectively, by:

$$\begin{aligned} \mathbf{N} &= \mathbf{L} \cos \alpha_g + \mathbf{D} \sin \alpha_g \\ \mathbf{T} &= \mathbf{L} \sin \alpha_g - \mathbf{D} \cos \alpha_g \end{aligned} \tag{5}$$

The tangential force plays a major role in generating power; indeed, **T** is the only force which is able to generate a torque at the shaft. As the lift contribution is greater than the drag one, the torque is oriented according to the direction of rotation generating power. Conversely, when the lift stall occurs, the lift contribution is negligible and the torque will be in disagreement with the direction of rotation.
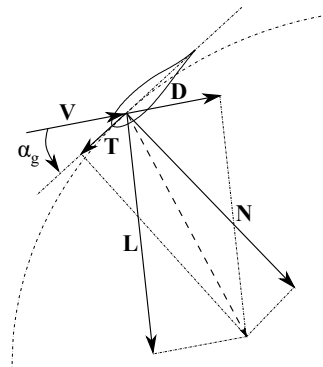
Figure 3. Aerodynamic forces on a VAWT blade cross section.

3. Case Study

In the present context, a 2D model of an H-Darrieus rotor was analysed. The chosen airfoil was the NACA 0018 with a chord c of 0.1 m. The blades were positioned at the radius equal to 0.5 m from the shaft with an aspect ratio equal to 10.

In order to capture 3D vortical structures, the computational grid required a spatial refinement in both axial and normal directions. Typically, these computational grids are characterized by more than 80 million elements with a high computational effort. In this work the three-dimensional effects could be neglected in the middle plane allowing a much more affordable 2D analysis. The geometrical and operational properties are summarized in Table 1.

Table 1. Geometrical and operational properties of the VAWT under study.

Parameter	Value
Number of blades, n	3
Radius, R (m)	0.5
Span length, b (m)	1
Swept area, A (m^2)	1
Chord/radius ratio, $\frac{c}{R}$	0.1
Airfoil	NACA 0018
Solidity, $\sigma\left(\frac{Nc}{R}\right)$	0.6
Tip-speed ratio (TSR), λ	1.25
Asymptotic wind velocity, $V_\infty\left(\frac{m}{s}\right)$	7
Global Reynolds number $\left(\frac{\rho V_\infty c}{\nu}\right)$	1×10^5
Rotational speed, $\Omega\left(\frac{rad}{s}\right)$	17.4533

4. Methodology

In this section, we address the methodology used to define a variable-pitch law that improves the power efficiency of the turbine.

We considered eight azimuthal positions, equally spaced $(\Delta\theta = 45°)$, in which the operating conditions were computed (V, Re, M, α). For each operating condition, airfoil drag polars were computed by means of the panel method X-Foil [33]. The effective angle of attack $\left(\alpha_{eff}\right)$ was chosen in order to maximize the steady aerodynamic efficiency and generate an anticlockwise torque. The pitch angle $\left(\alpha_p\right)$ was defined as the difference between the α_{eff} and α_g:

$$\alpha_p = \alpha_{eff} - \alpha_g \tag{6}$$

A cubic spline was used to fit the values of α_p defining the variable-pitch law.

4.1. Steady Polar Airfoil

As reported in Section 2, the tangential component of the aerodynamic force produced a torque on the shaft, which could be synchronous with the turbine motion. Therefore, a

positive contribution of the tangential force was obtained by reducing the drag contribution and increasing the lift one, as evidenced in Equation (5). Namely, the airfoil should operate at the effective angles of attack which maximize aerodynamic efficiency, defined as:

$$E_{max} = \frac{C_l(\alpha_{eff})}{C_d(\alpha_{eff})} \tag{7}$$

where C_l and C_d are defined as

$$\begin{aligned} C_l &= \frac{L(\alpha_{eff})}{\frac{1}{2}\rho V^2 S} \\ C_d &= \frac{D(\alpha_{eff})}{\frac{1}{2}\rho V^2 S} \end{aligned} \tag{8}$$

where L and D are the lift and drag forces of the airfoil, V is the relative speed, and S is the reference surface defined as the product of c for a unit length. The time history of aerodynamic forces is influenced by the variation in time of α_g, due to flow unsteadiness. Therefore, the computational overhead deriving from the computation of α_{eff} at each azimuthal position, shown in Figure 4, was reduced by assuming the flow steady.
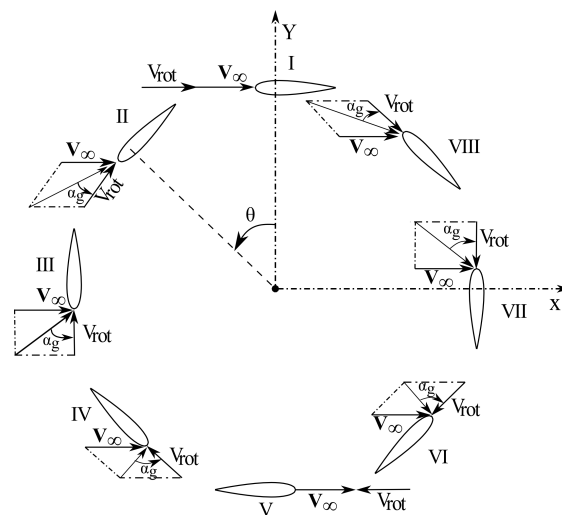
Figure 4. Velocity triangles and blade orientation at eight azimuthal positions.

Obviously, the α_{eff} values represent a conservative solution in the dynamic case because, considering the dynamic polar of the airfoil, the maximum aerodynamic efficiency is obtained at angle of attack values greater than those obtained in the static case. In order to find α_{eff}, the airfoil polars were computed by using the potential solver X-Foil. Airfoil shape, local Reynolds, and Mach numbers were input variables at each azimuthal position adopting the following relations:

$$\begin{aligned} Re &= \frac{\rho V(\theta)c}{\mu} \end{aligned} \tag{9}$$

$$\begin{aligned} M &= \frac{V(\theta)}{a} \end{aligned} \tag{10}$$

where V is the relative speed that was computed by means of Equation (1) assuming $\mathbf{v} = 0$, μ is the dynamic viscosity and a is the speed of sound at sea level. In Table 2 are reported the operating conditions for the azimuthal positions.

Table 2. Operating conditions at the eight azimuthal positions.

	θ	V	R_e	M
First position	0°	15.73	1.1×10^5	0.046
Second position	45°	14.54	1.0×10^5	0.04
Third position	90°	11.19	7.6×10^4	0.03
Fourth position	135°	6.23	4.2×10^4	0.02
Fifth position	180°	1.7	1.7×10^4	0.005
Sixth position	225°	6.23	4.2×10^4	0.02
Seventh position	270°	11.19	7.6×10^4	0.03
Eighth position	315°	14.54	1.1×10^5	0.04

The operating conditions at the second, third, and fourth azimuthal positions were similarly obtained at the eighth, seventh and sixth azimuthal positions, respectively. By examining Figure 4, the relative velocity is equal for points along the blade trajectory symmetrically placed with respect to the y-axis. In addition, the airfoil is symmetric, whereby only the airfoil polars at the first four azimuthal positions need to be computed. Furthermore, since the relative speed at the fifth position was close to zero, α_{eff} was imposed equal to zero to avoid an additional increase of the drag. In Figure 5, the airfoil drag polars computed at the first, second, third, and fourth azimuthal positions are reported.
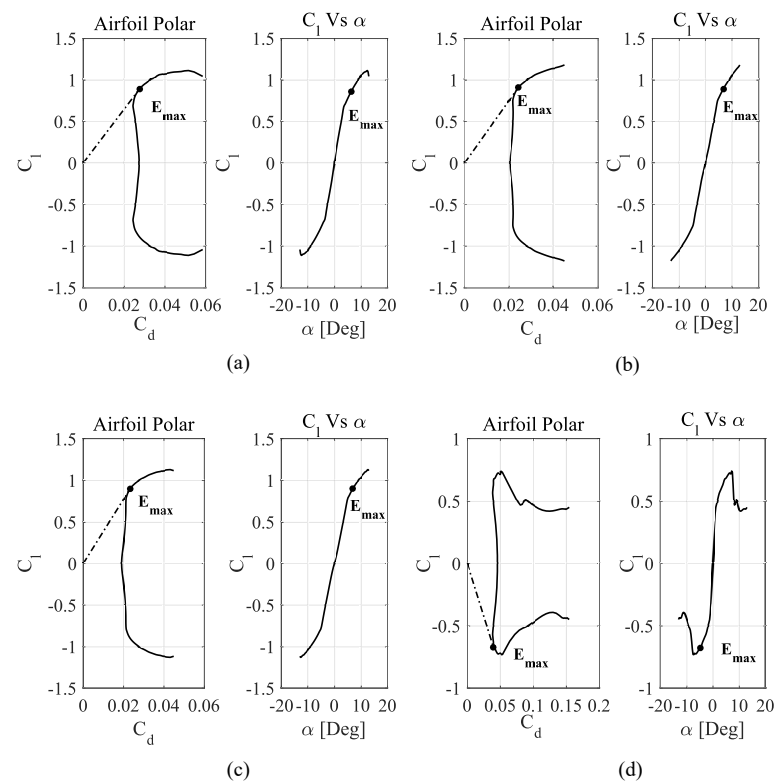
Figure 5. Airfoil polars at azimuthal positions: (**a**) first azimuthal position; (**b**) second azimuthal position; (**c**) third azimuthal position; (**d**) fourth azimuthal position.

The condition of maximum aerodynamic efficiency (E_{max}) was obtained graphically by intersecting the airfoil polar with the tangent curve, as shown in Figure 5. In Table 3, the values of α_{eff} at the azimuthal positions are reported. The sign of α_{eff} was positive for azimuthal positions in the range $0° \leq \theta \leq 180°$, while it was negative in the range $180° \leq \theta \leq 360°$. As a result, tangential forces created an anticlockwise torque, which was compliant with the turbine motion.

Table 3. Values of α_{eff} at the eight azimuthal positions.

	θ	α_{eff}
First position	0°	7°
Second position	45°	7°
Third position	90°	6.5°
Fourth position	135°	4.5°
Fifth position	180°	0°
Sixth position	225°	−4.5°
Seventh position	270°	−6.5°
Eighth position	315°	−7°

4.2. Variable-Pitch Law

The geometrical difference between α_{eff} and α_g at eight azimuthal positions is shown in Figure 6. The α_g was computed using Equation (2), and the resulting values are reported in Table 4.
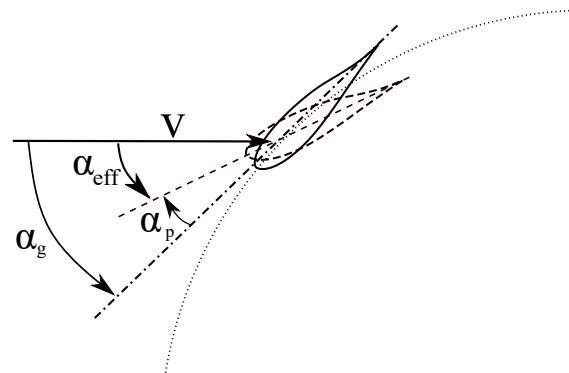
Figure 6. Pitching motion of the airfoil.

Table 4. Values of α_g at the eight azimuthal positions.

|	θ	α_g
First position	0°	0°
Second position	45°	19.89°
Third position	90°	38.73°
Fourth position	135°	52.6°
Fifth position	180°	0°
Sixth position	225°	−52.65°
Seventh position	270°	−38.73°
Eighth position	315°	−19.89°

As shown in Figure 6, α_p represents the angle by which the airfoil has to rotate in order for α_g to be exactly equal to the α_{eff} at each azimuthal position. In Table 5, the values of α_p at eight azimuthal positions are reported.

The pitch law was obtained by fitting a cubic spline interpolator through α_p. In particular, the Hermite interpolation implemented in Matlab software [34] was used. In order to ensure a unique solution, and to generate a periodic trajectory, at the spline end points, the same value of the first derivative ($\frac{\sqrt{2}}{2}$) was imposed. The pitch law is shown in Figure 7b, while a comparison between the variation of α_{eff} and α_g as a function of the azimuthal position is illustrated in Figure 7a.

Table 5. Values of α_p at the eight azimuthal positions.

	θ	α_p
First position	0°	7°
Second position	45°	−12.90°
Third position	90°	−32.23°
Fourth position	135°	−48.15°
Fifth position	180°	0°
Sixth position	225°	48.15°
Seventh position	270°	32.23°
Eighth position	315°	12.90°
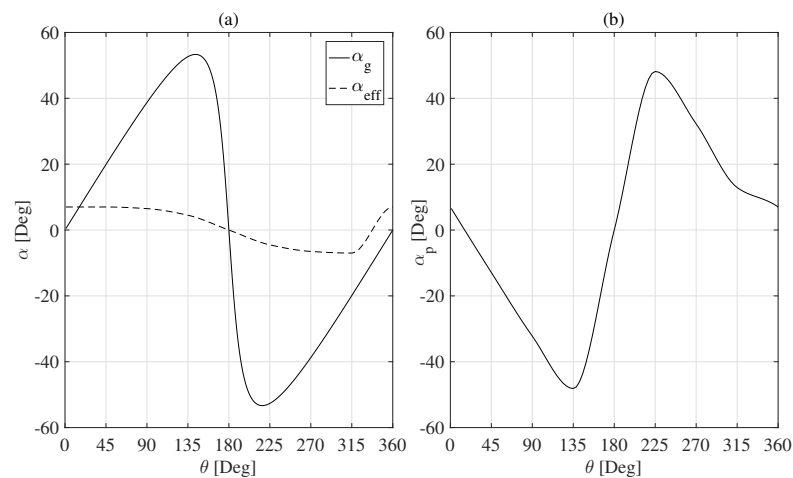
Figure 7. (**a**) Variation of α_g and α_{eff} vs. azimuthal positions; (**b**) pitch law.

In Figure 8, the layout of the blade orientation is reported. The methodology described above was implemented in Matlab by generating an automatic procedure. Therefore, the user obtains as output the variable-pitch law in real time by providing as input the chosen airfoil, the radius, and the operating conditions of the turbine. Considering the motion of the turbine without the airfoil pitching, a power loss for each blade during the entire revolution was expected. This behaviour was due to the steep variation of α_g, as observed in Figure 7a.
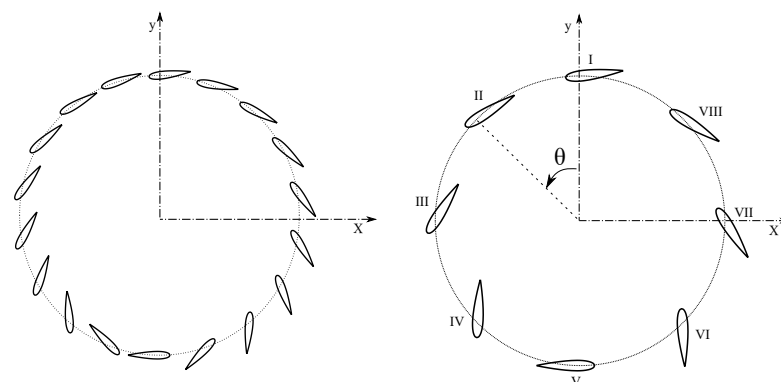
Figure 8. (**left**) Layout of the blade orientations during a period of revolution; (**right**) layout of the blade orientations at the same positions as in Figure 4.

5. CFD Simulation

5.1. Computational Domain

The computational domain used to simulate the motion of the rotor is reported in Figure 9.

The height and length of the domain were set equal to 72.5*c* and 225*c*, respectively, in order to guarantee a full development of the wake [35]. To simulate both blade and pitch motions, a domain partition into both fixed (Figure 9E,F) and rotating regions was required. The rotating regions were further divided into: (i) three circular regions whose centres were at the quarter of the chord of each airfoil, namely, *blade region* (Figure 9A–C) and (ii) a ring that included the three circular regions, namely, *rotor* (Figure 9D). That way, all the regions were able to rotate around the shaft and, at same time, the circular regions were able to turn around their centres respecting the pitch law. In the solver Ansys Fluent® [36], the most accurate method for simulating flows in multiple moving reference frames is the sliding mesh model. An interface condition was imposed at the boundaries of the rotating regions, while no slip condition was imposed at the boundaries of the airfoil. At the upstream and downstream of the fixed region, velocity inlet and pressure outlet conditions were assigned; at the top and bottom of the fixed region, symmetry conditions were adopted. The pitch law was developed by means of an ad hoc user-defined function (UDF) [37] compiled within the solver Fluent.
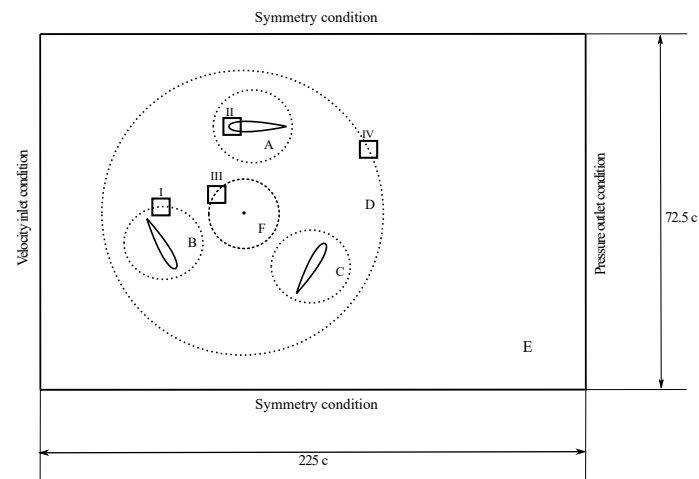
Figure 9. Layout of the computational domain (not at scale). Rotating regions: (**A–D**); fixed regions: (**E,F**); dot: interfaces between domains; square: details of computational domain.

5.2. User-Defined Function

The user-defined functions are C functions which are interpreted or compiled in commercial software Ansys Fluent, and they can be dynamically loaded in the software tool. These functions allow software customisation to simulate a phenomenon of interest by better approximating reality.

In this work, the *DEFINE_ZONE_MOTION* UDF was adopted to simulate the airfoil pitch motion during the rotation. Namely, this function allows a rigid translation and rotation of computational domain regions either with respect to the basic reference system or with respect to a generic point. The arguments of the UDF are the motion components such as: rotational axis origin vector, rotational speed, rotation axis direction vector, and translational velocity vector. In this work, the circumferences centred at the *c*/4 of each airfoil were chosen as the regions of the computational domain. This choice was taken to simplify the components of the pitch motion to be assigned. In that way, at each time step and for each airfoil, the coordinates of points at *fracc*4 represented the rotation axis origin vector. These were evaluated by:

$$
\begin{aligned}
x_{\frac{c}{4}}(t) &= R\cos(\theta_t + \theta_0) \\
y_{\frac{c}{4}}(t) &= R\sin(\theta_t + \theta_0) \\
z_{\frac{c}{4}}(t) &= 0
\end{aligned}
\tag{11}
$$

where θ_t and θ_0 are the azimuthal positions of each blade at the current time t and at time $t = 0$, respectively. The values of rotational speed ω_b were evaluated at each time step according to the variable-pitch law. In particular, we discretized the variable-pitch law in accordance with the time step used in the simulation (Δt). The values of ω_b were estimated by means of the finite difference method, as reported in the following equation:

$$\omega_b = \frac{\alpha_{p_{t-1}} - \alpha_{p_t}}{\Delta t} \tag{12}$$

where $\alpha_{p_{\Delta t-1}}$ and $\alpha_{p_{\Delta t}}$ are the values of the pitch angle of each blade at the previous time ($t - 1$) and at the current step.

In Figure 10, the flow chart of *DEFINE_ZONE_MOTION* is reported.
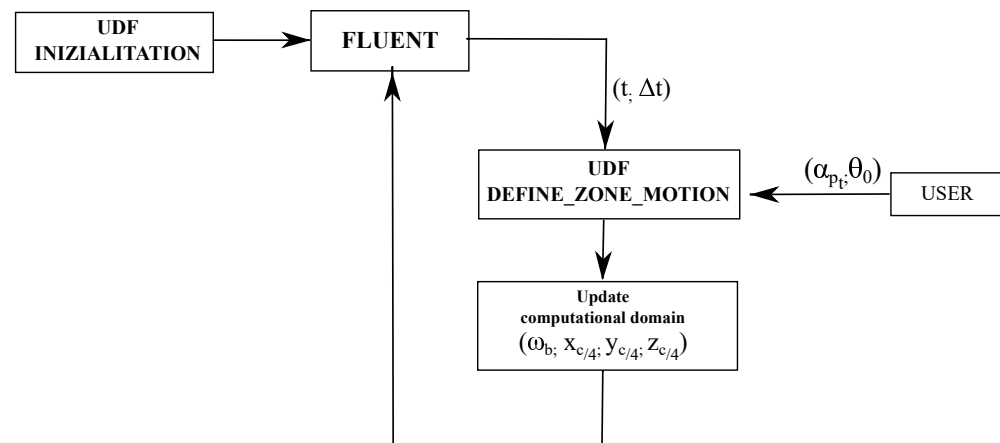
Figure 10. Flow chart of *DEFINE_ZONE_MOTION* (UDF).

5.2.1. Numerical Method

The numerical simulations presented in this paper were performed by adopting the commercial CFD code Fluent. The unsteady Reynolds averaged Navier–Stokes equations (U-RANS) with the $k - \omega SST$ turbulence model was used. The equations were spatially discretized using the finite-volume method and the pressure-based solver was adopted in the solution phase. The coupling between pressure and velocity was achieved by using the coupled algorithm. Convective terms were discretized by adopting the second-order upwind scheme, such as the transport term, momentum, and turbulence. Diffusion terms were central-differenced and were always second-order accurate. Cell gradients were computed by using the least-squares cell-based algorithm [24]. Iterative convergence was obtained when all the variable residuals were less than 10^{-5} in magnitude [38]; generally, 20 iterations on average were required for convergence. A grid convergence solution was obtained when the mean airfoil torque coefficient between two time periods did not change by more than 0.1% [39]. In addition, a temporal discretization was performed using the first-order implicit Euler method that allowed a larger region of stability through diffusive and convective stability constraints [40].

5.2.2. Meshing Strategy

The discretization of the computational domain is a challenging task, especially at low TSR $<< 5$, due to the presence of complex flow regimes [38].

In the present context, a hybrid mesh was adopted to partition the computational domain in order to reduce the number of required elements. As shown in Figure 11, the fixed and rotating domains were discretized using a structured quadrilateral and unstructured triangular elements, respectively.

In addition, layered elements were adopted in the near-wall region of the airfoils in order to correctly evaluate the viscous effects and the detachment of the flow vein. The boundary layer thickness was estimated by means of the following equation:

$$\delta = \frac{c}{\sqrt{Re}} \qquad (13)$$

where the global Reynolds number was computed from Equation (9) assuming the asymptotic wind velocity $\mathbf{V}_\infty$. In order to resolve the viscous sublayer, the height of the first layer guaranteed the condition $y^+ \leq 1$ [36,41]. In that case, the y^+ was set equal to 0.6 to ensure that up to six cells were present in the viscous sublayer. At the sliding interface, both quadrilateral and triangular elements had the same edge size to minimize the interpolation error between the two zones [36].

(a)

(b)

(c)

(d)
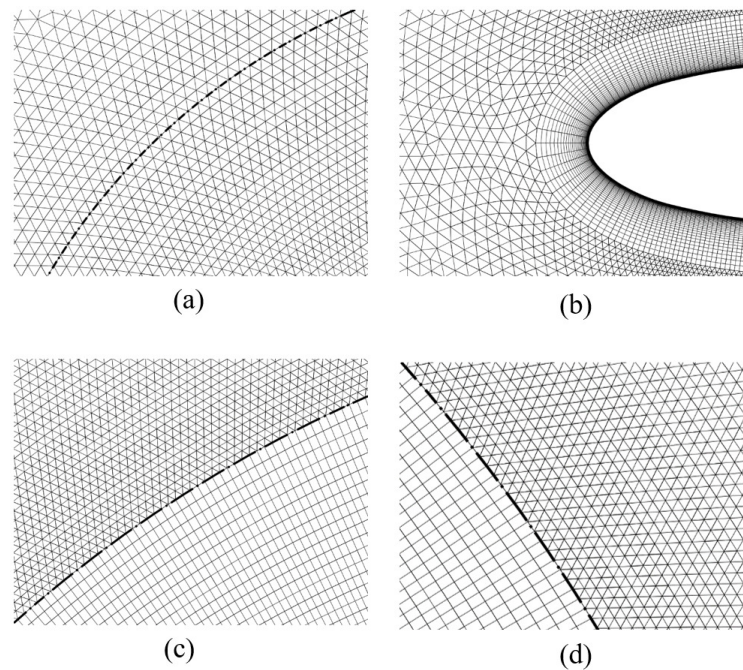
Figure 11. Details of the discretized computational domain: (**a**) interface rotor and blade region (I in Figure 9); (**b**) boundary layer (II in Figure 9); (**c**) interface rotor and fixed domain (III in Figure 9); (**d**) interface rotor and fixed domain (IV in Figure 9).

5.2.3. Spatial Resolution Study

To describe the flow structure that originates from the flow field (vortices, wake, etc.), the time step and the mesh size must be small enough [39,42]. Three computational domains (G_I–G_{III}) were analysed with different cell densities, as reported in Table 6, to evaluate the effect of spatial resolution on the numerical solution.

Table 6. Details of the computational domains.

Node Numbers	G_I	G_{II}	G_{III}
Airfoil	208	416	416
Layers	40	40	40
Inlet	206	412	824
Outlet	206	412	824

This approach allowed a local mesh refinement where vortical structures were expected. In order to reduce the computational overhead, the turbine motion without the pitch law was analysed. As the optimal computational time step was not a priori known, we set it equal to 1×10^{-4} in order to guarantee a unit Courant number. It was evaluated based on the free stream velocity and the minimum element size among the computational domains, i.e., the most critical condition for the computational stability. In addition, this

time step guaranteed both convergence with respect to the convective flux and sliding mesh criteria [36].

The results of the three analyses confirmed that, by using of a coarse computational domain, an underestimation of the mean airfoil torque coefficient C_m was obtained, due to a poor spatial discretization on the airfoil surfaces, as shown in Figure 12.
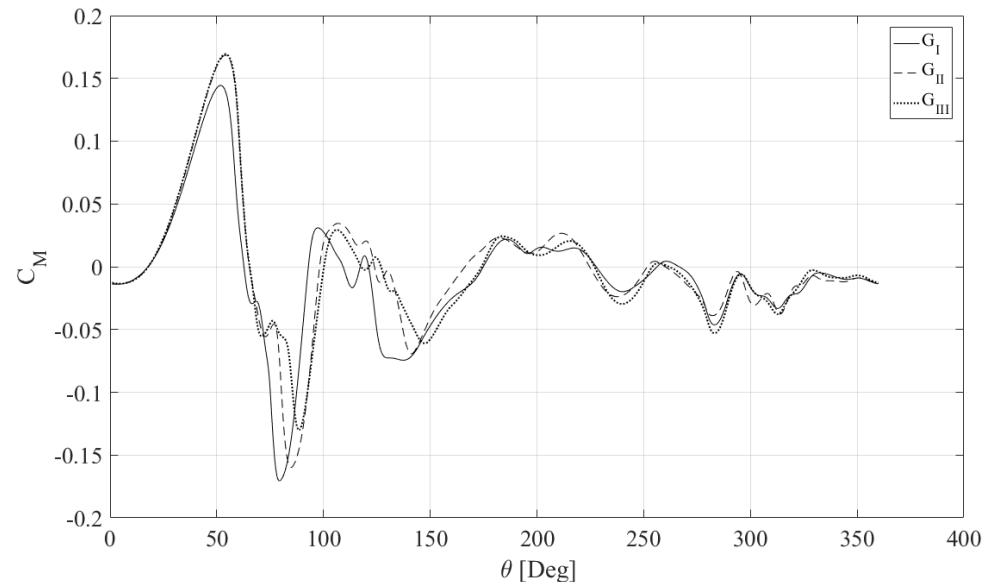

Figure 12. Spatial independence.

The coefficient C_M of the total torque was defined as:

$$C_M = \frac{M}{\frac{1}{2}\rho V^2 RA} \tag{14}$$

where M is the aerodynamic torque generated by the blade calculated with respect to the rotation axis, and A is the reference surface defined as the product between diameter and height of the turbine.

The coarse computational domain did not provide a good evaluation of detachment phenomena, returning higher values of the adverse gradient pressure that produced a high drop of the torque coefficient. Conversely, by adopting a medium or fine computational domain, the results were extremely close and thus, utilizing a smaller element size did not increase the accuracy of the predicted results. Since the difference between the results of the medium and fine computational domain was less of 5%, we used the medium computational domain to analyse the motion thereby reducing the computational effort.

5.2.4. Temporal Resolution Study

The choice of a suitable time step plays a main role to obtain a correct description of vortical structures and wake prediction. The time step was chosen in order to guarantee the lowest computational effort without compromising the accuracy of the results [42]. To assure a time independency of the numerical solution, three different simulations using the medium computational domain at $\Delta t = 10^{-3}, \Delta t = 10^{-4}$, and $\Delta t = 10^{-5}$ were carried out. By assuming a turbine rotation of 17.4533 rad/s for these cases, corresponding turbine rotation steps equal to $\Delta\theta = 1°, \Delta\theta = 0.1°$, and $\Delta\theta = 0.01°$ were obtained, respectively.

The variation of the torque coefficients as a function of the azimuthal position θ, for the above defined values of Δt, is shown in Figure 13.

It can be observed that for time steps $\Delta\theta = 1°$ and $\Delta\theta = 0.1°$ the difference between the results became negligible. Hence, a time step $\Delta\theta = 0.1°$ was adopted for all the simulations. One full rotation took about 24 h utilizing a medium computational domain, $\Delta t = 10^{-4}$, and using a parallel computing architecture based on a 16-core INTEL

Xeon Xeon E5 2.9 GHz. Confidently, in order to predict a single torque coefficient value, six full rotations were performed.
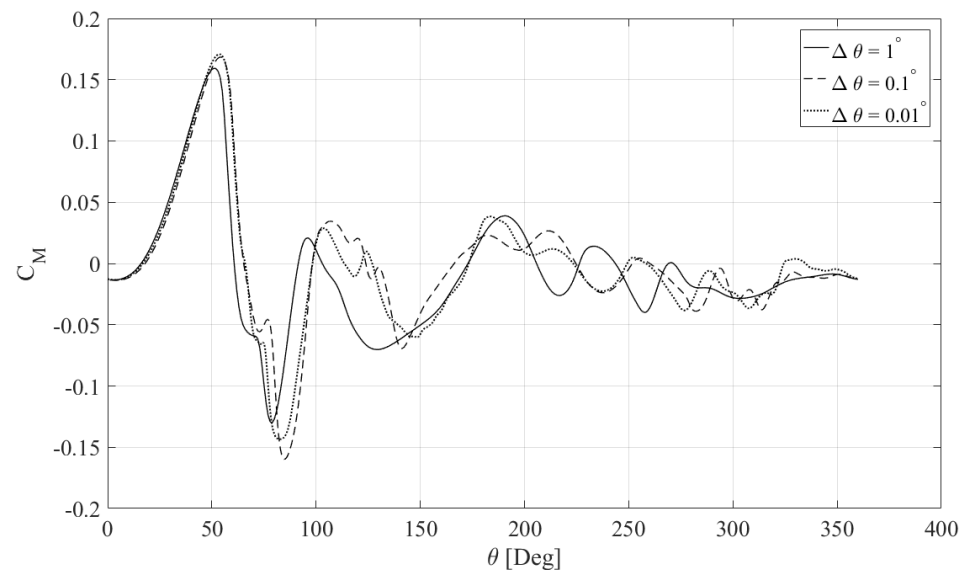
Figure 13. Temporal independence.

6. Results

In this section, the 2-D numerical simulations are reported. In particular, the effects of the variable-pitch law on the VAWT performance are assessed. In Figure 14, the instantaneous torque coefficient obtained with the pitch law (Case 1) is compared to a fixed pitch (Case 0).
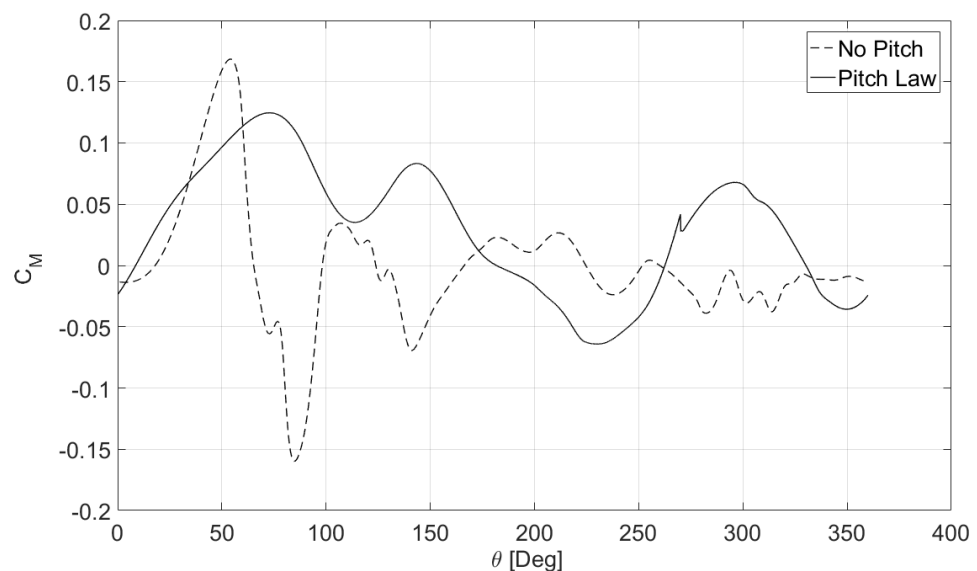
Figure 14. Instantaneous torque coefficient versus azimuthal position: case without pitch law (Case 0) and with pitch law (Case 1).

As expected, the behaviour obtained in Case 0 was typical of a highly unsteady aerodynamic field characterized by the existence of vortical structures generated by dynamic stall. Instead, in Case 1, the dynamic stall was delayed as it appears by looking at the behaviour of C_M in Figure 14, where the sudden loss of C_M is not present. Those different behaviours are highlighted by the contours of the pressure and velocity fields shown in Figure 15 and Figure 16, respectively. In both cases, in the range $0° < \theta < 10°$, the static pressure fields around the airfoil showed the flow fully attached to the airfoil (Figure 15a,b).

Two main reasons caused this behaviour: (i) the airfoil worked at angles of attack far from dynamic stall conditions; (ii) the aerodynamic field in the upstream phase ($350° < \theta < 10°$) was not influenced by the wake generated by other airfoils, as confirmed by the velocity field reported in Figure 16a,b. Furthermore, pressure fields obtained at $0° < \theta < 10°$, represented in Figure 15a,b, showed an increment of the static pressure difference between the pressure side and suction side of the airfoil in Case 1. This caused the increment of C_M compared to Case 0, as shown in Figure 14. In the remaining azimuthal range, the phenomena occurring in Case 0 and Case 1 were different from each other. In Case 0, the values of the angle of attack increased in the range $10° < \theta < 64°$.

Moreover, a reversed flow occurred at the trailing edge due to the rapid airfoil motion, as shown in Figures 15 and 16. In the same range, the LEV was already formed, delaying the lift stall to an angle greater than that of the static stall. The LEV increased the depression on the suction side raising the difference in static pressure between the surfaces of airfoil. In that way, the lift force increased compared to the static case. The maximum difference of static pressure was obtained at $\theta \cong 64°$ since, as shown in Figures 15d and 16d, the LEV spanned over the whole suction side of the airfoil. At this value of θ, namely θ^*, a peak of instantaneous torque coefficient was obtained. For $\theta > \theta^*$, the angle of attack achieved the dynamic stall angle value and the LEV detached from the airfoil causing a sudden loss of lift, as shown in Figure 14. Since the variation of α_g was steep, there was a considerable delay in the flow reattachment. Only when the airfoil returned to the upstream phase did the flow reattach to the airfoil, as shown in Figures 15e–i and 16e–i. Therefore, in that range, the C_M values oscillated around the zero value. On the other hand, in Case 1, the flow was attached to the body until the section blade was in the range $10° < \theta < 170°$, as shown in Figure 15b–f. Currently, only in the range $170° < \theta < 210°$ did separation occur at the trailing edge, and a simultaneous growth of LEV was observed. This behaviour is visible in Figures 15f–h and 16f–h. In Case 1, the flow was quasi-steady, and the airfoils worked at a low angle of attack; at the remaining azimuthal positions, the flow reattached, producing an increase of C_M values, as shown in Figures 15i and 16i.

As we expected, the maximum value of C_M was obtained in Case 0. This behaviour was due to the methodology used to determine the effective angle. In fact, the static polar used underestimated the maximum efficiency condition compared to the dynamic polar. Nevertheless, the improvement in performance achieved adopting the variable pitch was evident when observing the behaviour of the global torque coefficient of the three blades versus the azimuthal positions reported in Figure 17. For Case 0, the average torque coefficient value C_{M_a} was equal to -0.16 compared to a C_{M_a} value obtained in Case 1 equal to 0.11 with an improvement of 0.27. The average value of the power coefficient C_{p_a} was defined as:

$$C_{p_a} = \frac{\int_0^{2\pi} \frac{C_{M_g} * \omega}{V_\infty}\, d\theta}{2\pi} = \frac{\int_0^{2\pi} C_p\, d\theta}{2\pi}. \tag{15}$$

where C_{M_g} is the torque coefficient of the three blades. In Case 0, C_{p_a} was equal to -0.026. As is known in the literature [43,44], the solidity, the Reynolds number, and the cord length identify a class of turbine with the same performance. In particular, Brusca et al. [43] studied the performances of turbines characterized by airfoil section NACA 0018 at low Reynolds numbers, a high solidity and different TSRs. These geometrical and operational properties identified the same class of turbine model presented in this work. In the literature, there are no experimental studies on this class of turbines at low TSRs because they typically do not produce power but absorb it.

Consequentially, in order to validate the performance obtained with the proposed numerical modelling, we compared the C_{pa} obtained in this work with the one obtained by Brusca et al. at the same TSR. The percent error committed was estimated by means of the following equation:

$$\%_{error} = \frac{C_{p_a}{}^{Brusca} - C_{p_a}}{C_{p_a}{}^{Brusca}} * 100 \tag{16}$$

and it was equal to 12%.

Globally, the turbine without the pitch law did not produce energy but absorbed it, while, in Case 1, the turbine generated an average power equal to 23 W with C_{p_a} equal to 0.27.
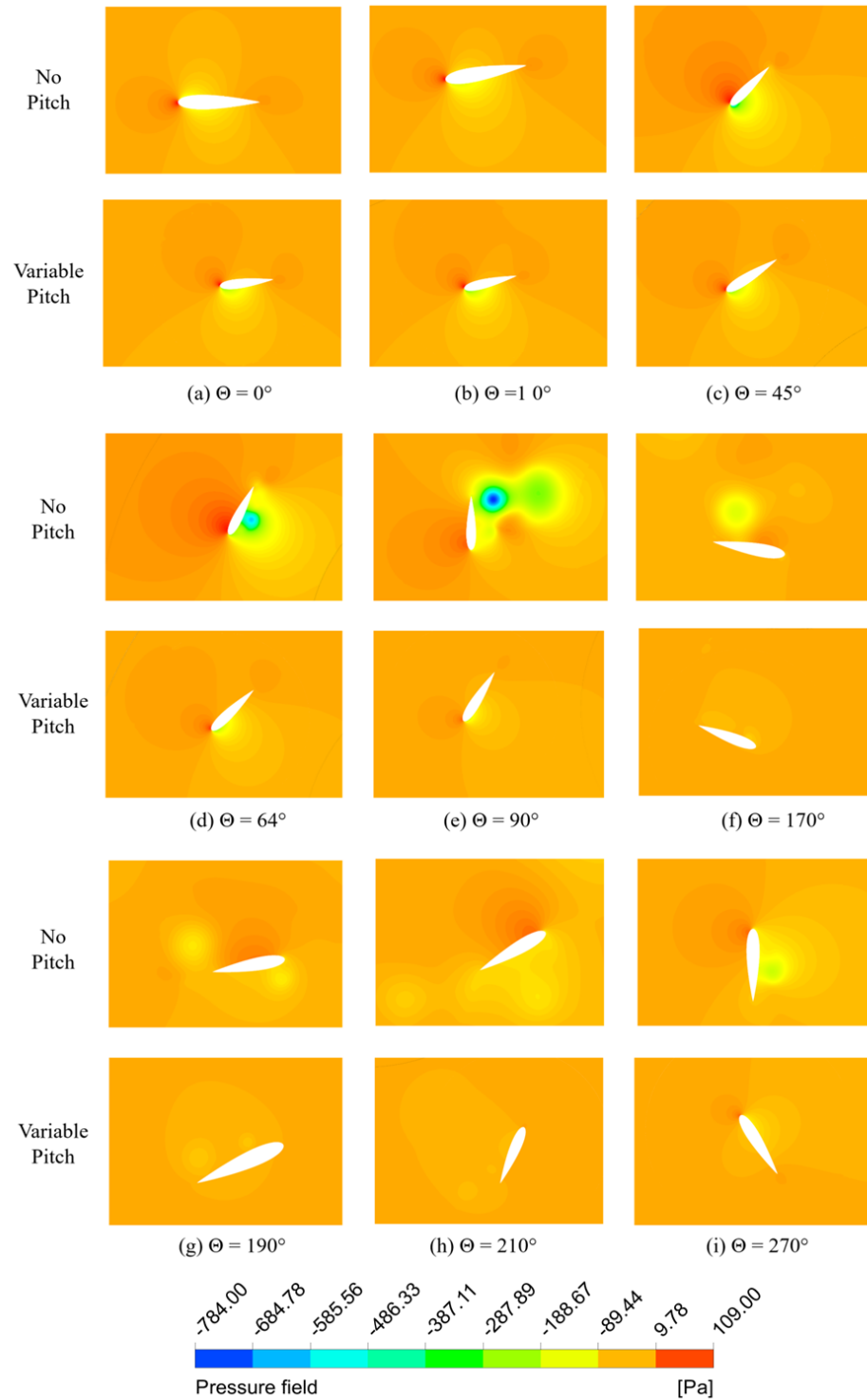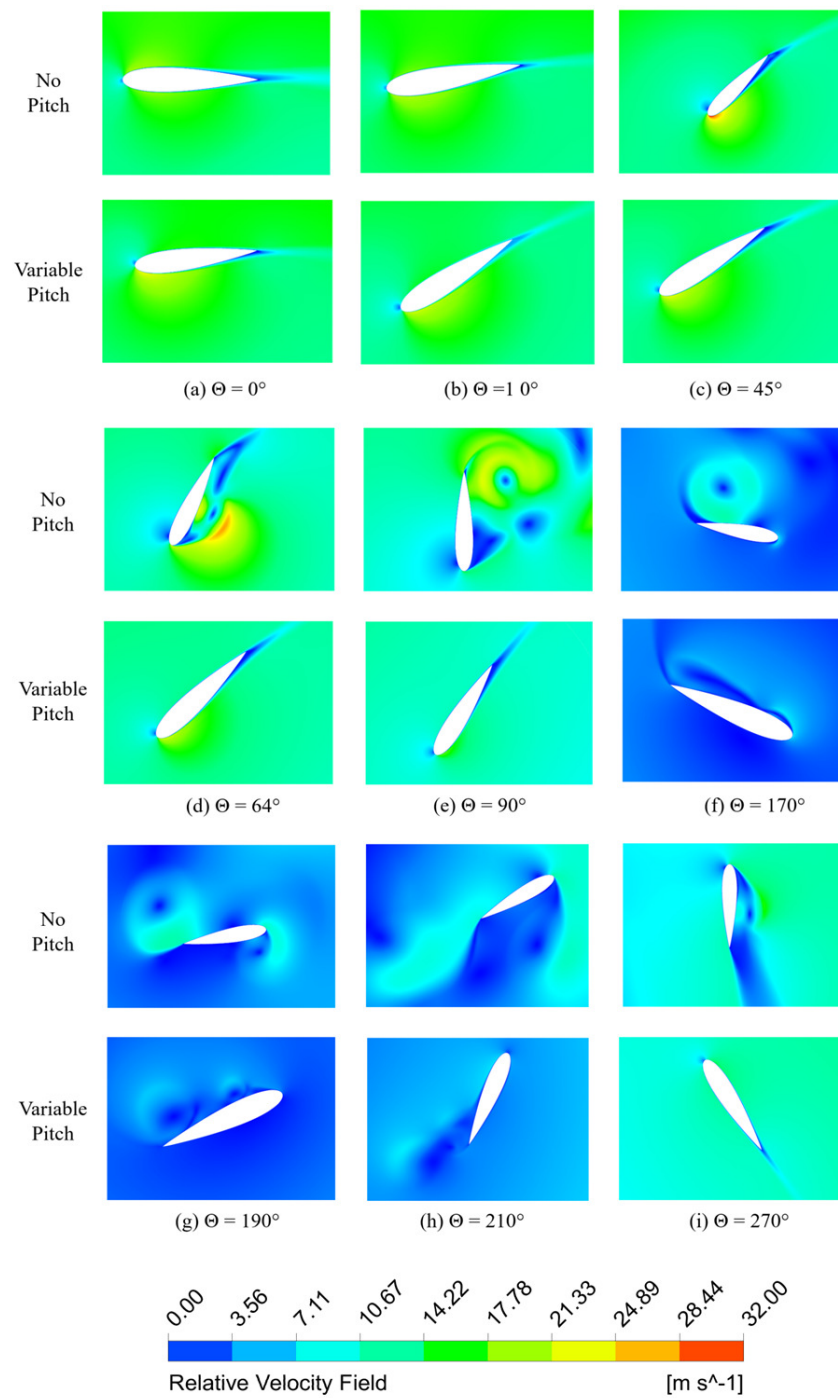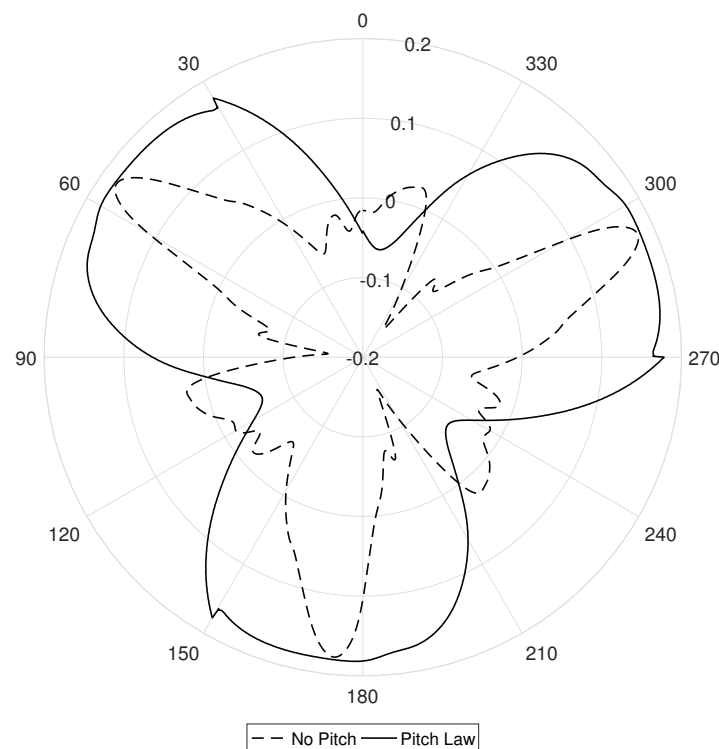

Figure 15. Pressure field around the no-pitch and variable-pitch blades at different azimuthal positions.

Figure 16. Relative velocity field around the no-pitch and variable-pitch blades at different azimuthal positions.

Figure 17. Torque coefficient versus azimuthal position: case without pitch law ($C_{Mmedium} = -0.16$) and with pitch law ($C_{Mmedium} = +0.11$).

7. Conclusions

Vertical-axis wind turbines represent a suitable technology to convert kinetic energy, extracted from the wind, into electric energy. However, the presence of unstable aerodynamic phenomena such as dynamic stall, deep stall, and blade–wave interaction results in a lower efficiency of such turbines. Several methodologies have been proposed in literature to improve the aerodynamic efficiency of wind turbines, but they turn out to be computationally inefficient. In this study, a new efficient methodology to define a variable-pitch law which improves the performance of an H-Darrieus turbine was implemented using an automatic procedure. It was based on the determination of the angles of attack in eight azimuthal positions where the maximum steady aerodynamics efficiency condition was satisfied. In order to validate this methodology, the effects of a variable pitch on the torques of a 2D model of the H-Darrieus turbine were analysed. In particular, a U-RANS analysis with a $K - \omega\ SST$ turbulent model was carried out. The sliding-mesh technique was used to simulate the pitch motion during the cycle rotation.

A comparison of the results obtained by applying the pitch law as opposed to a no-pitch-law condition highlighted how the pitch law actually delayed the dynamic stall improving the aerodynamic performance considerably. The mean value of the power coefficient obtained by implementing the pitch law results significantly increased. Obviously, the global angle of attack obtained with the proposed methodology represents a suboptimal solution in the dynamic case because the dynamic maximum aerodynamic efficiency is obtained at values of the angle of attack greater than the static case. However, this methodology is more versatile than those already present in the literature because it does not require optimization and could be implemented in hardware to modify the pitch law in real time, following different asymptotic wind conditions.

Author Contributions: Conceptualization, C.R. and L.I.; methodology and software, C.R. and D.D.S.; validation, C.R. and L.I.; formal analysis, C.R. and D.D.S.; resources, A.V.; data curation, C.R., D.D.S. and G.P.; writing, C.R. and L.I.; writing and editing, C.R. and L.I.; review, G.P. and A.V.; supervision, A.V. All authors have read and agreed to the published version of the manuscript.

References

1. Wilkes, J.; Moccia, J.; Arapogianni, A.; Dragan, M.; Plytas, N.; Genachte, A.; Guillet, J.; Wilczek, P. *The European Offshore Wind Industry Key 2011 Trends and Statistics*; Report of European Wind Energy Association; European Wind Energy Association: Brussels, Belgium, 2012.
2. Pryor, S.; Barthelmie, R. Climate change impacts on wind energy: A review. *Renew. Sustain. Energy Rev.* **2010**, *14*, 430–437. [CrossRef]
3. Stathopoulos, T.; Alrawashdeh, H.; Al-Quraan, A.; Blocken, B.; Dilimulati, A.; Paraschivoiu, M.; Pilay, P. Urban wind energy: Some views on potential and challenges. *J. Wind. Eng. Ind. Aerodyn.* **2018**, *179*, 146–157. [CrossRef]
4. Al-Quraan, A.; Stathopoulos, T.; Pillay, P. Comparison of wind tunnel and on site measurements for urban wind energy estimation of potential yield. *J. Wind. Eng. Ind. Aerodyn.* **2016**, *158*, 1–10. [CrossRef]
5. Keegan, M.H.; Nash, D.H.; Stack, M.M. On erosion issues associated with the leading edge of wind turbine blades. *J. Phys. D Appl. Phys.* **2013**, *46*, 383001. [CrossRef]
6. Mishnaevsky, L.; Hasager, C.B.; Bak, C.; Tilg, A.M.; Bech, J.I.; Doagou Rad, S.; Fæster, S. Leading edge erosion of wind turbine blades: Understanding, prevention and protection. *Renew. Energy* **2021**, *169*, 953–969. [CrossRef]
7. Carraro, M.; Vanna, F.D.; Zweiri, F.; Benini, E.; Heidari, A.; Hadavinia, H. CFD Modeling of Wind Turbine Blades with Eroded Leading Edge. *Fluids* **2022**, *7*, 302. [CrossRef]
8. Eriksson, S.; Bernhoff, H.; Leijon, M. Evaluation of different turbine concepts for wind power. *Renew. Sustain. Energy Rev.* **2008**, *12*, 1419–1434. [CrossRef]
9. Ferreira, C.S.; Van Kuik, G.; Van Bussel, G.; Scarano, F. Visualization by PIV of dynamic stall on a vertical axis wind turbine. *Exp. Fluids* **2009**, *46*, 97–108. [CrossRef]
10. Bos, R. Self-Starting of a Small Urban Darrieus Rotor. Strategies to Boost Performance in Low-Reynolds-Number Flows. Master's Thesis, TU Delft University, Delft, The Netherlands, 2012.
11. Wang, Y.; Sun, X.; Dong, X.; Zhu, B.; Huang, D.; Zheng, Z. Numerical investigation on aerodynamic performance of a novel vertical axis wind turbine with adaptive blades. *Energy Convers. Manag.* **2016**, *108*, 275–286. [CrossRef]
12. Huang, D.; Wu, G. Preliminary study on the aerodynamic characteristics of an adaptive reconfigurable airfoil. *Aerosp. Sci. Technol.* **2013**, *27*, 44–48. [CrossRef]
13. Bishop, K.L. The relationship between 3-D kinematics and gliding performance in the southern flying squirrel, Glaucomys volans. *J. Exp. Biol.* **2006**, *209*, 689–701. [CrossRef] [PubMed]
14. Swartz, S.; Iriarte-Diaz, J.; Riskin, D.; Tian, X.; Song, A.; Breuer, K. Wing structure and the aerodynamic basis of flight in bats. In Proceedings of the 45th AIAA Aerospace Sciences Meeting and Exhibit, Reno, NV, USA, 8–11 January 2007.
15. Ismail, M.; Vijayaraghavan, K. Investigation of flow over an oscillating airfoil for wind turbine application. In Proceedings of the Canadian Society for Mechanical Engineering (CSME) International Congress, Toronto, ON, Canada, 1–4 June 2014.
16. Gopalarathnam, A.; Broughton, B.A.; McGranahan, B.D.; Selig, M.S. Design of low Reynolds number airfoils with trips. *J. Aircr.* **2003**, *40*, 768–775. [CrossRef]
17. Mai, H.; Dietz, G.; Geißler, W.; Richter, K.; Bosbach, J.; Richard, H.; de Groot, K. Dynamic stall control by leading edge vortex generators. *J. Am. Helicopter Soc.* **2008**, *53*, 26–36. [CrossRef]
18. Paraschivoiu, I. *Wind Turbine Design with Emphasis on Darrieus Concept*; Polytechnic International Press: Montreal, QC, Canada, 2002.
19. Ahmed, M.R. Blade sections for wind turbine and tidal current turbine applications–current status and future challenges. *Int. J. Energy Res.* **2012**, *36*, 829–844. [CrossRef]
20. Howell, R.; Qin, N.; Edwards, J.; Durrani, N. Wind tunnel and numerical study of a small vertical axis wind turbine. *Renew. Energy* **2010**, *35*, 412–422. [CrossRef]
21. Paraschivoiu, I.; Trifu, O.; Saeed, F. H-Darrieus wind turbine with blade pitch control. *Int. J. Rotating Mach.* **2009**, *2009*, 505343. [CrossRef]
22. Rezaeiha, A.; Kalkman, I.; Blocken, B. Effect of pitch angle on power performance and aerodynamics of a vertical axis wind turbine. *Appl. Energy* **2017**, *197*, 132–150. [CrossRef]
23. Kiwata, T.; Yamada, T.; Kita, T.; Takata, S.; Komatsu, N.; Kimura, S. Performance of a vertical axis wind turbine with variable-pitch straight blades utilizing a linkage mechanism. *J. Environ. Eng.* **2010**, *5*, 213–225. [CrossRef]
24. Elkhoury, M.; Kiwata, T.; Aoun, E. Experimental and numerical investigation of a three-dimensional vertical-axis wind turbine with variable-pitch. *J. Wind. Eng. Ind. Aerodyn.* **2015**, *139*, 111–123. [CrossRef]
25. Hwang, I.S.; Lee, Y.H.; Kim, S.J. Optimization of cycloidal water turbine and the performance improvement by individual blade control. *Appl. Energy* **2009**, *86*, 1532–1540. [CrossRef]
26. Staelens, Y.; Saeed, F.; Paraschivoiu, I. A straight-bladed variable-pitch VAWT concept for improved power generation. In *ASME 2003 Wind Energy Symposium*; American Society of Mechanical Engineers: New York, NY, USA, 2003; pp. 146–154.

27. Li, Y.; Calisal, S.M. Three-dimensional effects and arm effects on modeling a vertical axis tidal current turbine. *Renew. Energy* **2010**, *35*, 2325–2334. [CrossRef]
28. Kirke, B.K. Evaluation of Self-Starting Vertical Axis Wind Turbines for Stand-Alone Applications. Ph.D. Thesis, Griffith University Australia, South East Queensland, Australia, 1998.
29. Amet, E.; MaÃŽtre, T.; Pellone, C.; Achard, J.L. 2D numerical simulations of blade-vortex interaction in a Darrieus turbine. *J. Fluids Eng.* **2009**, *131*, 111103–111115. [CrossRef]
30. Gordon, L.J. *Principles of Helicopter Aerodynamics*; Cambridge University Press: Cambridge, UK, 2016.
31. Wang, S.; Ingham, D.B.; Ma, L.; Pourkashanian, M.; Tao, Z. Numerical investigations on dynamic stall of low Reynolds number flow around oscillating airfoils. *Comput. Fluids* **2010**, *39*, 1529–1541. [CrossRef]
32. Hand, B.; Kelly, G.; Cashman, A. Numerical simulation of a vertical axis wind turbine airfoil experiencing dynamic stall at high Reynolds numbers. *Comput. Fluids* **2017**, *149*, 12–30. [CrossRef]
33. Drela, M.; Youngren, H. XFOIL 6.94 User Guide. 2001. Available online: http://web.mit.edu/drela/Public/web/xfoil/ (accessed on 24 December 2022).
34. MatLab, M. *The Language of Technical Computing*; The MathWorks, Inc.: Natick, MA, USA, 2012. Available online: http://www.mathworks.com (accessed on 24 December 2022).
35. Rezaeiha, A.; Kalkman, I.; Blocken, B. CFD simulation of a vertical axis wind turbine operating at a moderate tip speed ratio: Guidelines for minimum domain size and azimuthal increment. *Renew. Energy* **2017**, *107*, 373–385. [CrossRef]
36. Fluent, A. *12.0 Theory Guide*; Ansys Inc.: Canonsburg, PA, USA, 2009; Volume 5.
37. Fluent, A. *15.0 UDF Manual*; Ansys Inc.: Canonsburg, PA, USA, 2013.
38. Balduzzi, F.; Bianchini, A.; Maleci, R.; Ferrara, G.; Ferrari, L. Critical issues in the CFD simulation of Darrieus wind turbines. *Renew. Energy* **2016**, *85*, 419–435. [CrossRef]
39. Balduzzi, F.; Bianchini, A.; Ferrara, G.; Ferrari, L. Dimensionless numbers for the assessment of mesh and timestep requirements in CFD simulations of Darrieus wind turbines. *Energy* **2016**, *97*, 246–261. [CrossRef]
40. Ferziger, J.H.; Peric, M. *Computational Methods for Fluid Dynamics*; Springer Science & Business Media: Berlin, Germany, 2012.
41. Andersson, B.; Andersson, R.; Håkansson, L.; Mortensen, M.; Sudiyo, R.; Van Wachem, B. *Computational Fluid Dynamics for Engineers*; Cambridge University Press: Cammbridge, UK, 2011.
42. Almohammadi, K.; Ingham, D.; Ma, L.; Pourkashan, M. Computational fluid dynamics (CFD) mesh independency techniques for a straight blade vertical axis wind turbine. *Energy* **2013**, *58*, 483–493. [CrossRef]
43. Brusca, S.; Lanzafame, R.; Messina, M. Design of a vertical-axis wind turbine: How the aspect ratio affects the turbine's performance. *Int. J. Energy Environ. Eng.* **2014**, *5*, 333–340. [CrossRef]
44. Eboibi, O.; Danao, L.A.M.; Howell, R.J. Experimental investigation of the influence of solidity on the performance and flow field aerodynamics of vertical axis wind turbines at low Reynolds numbers. *Renew. Energy* **2016**, *92*, 474–483. [CrossRef]